Topological Entropy Bounds for Hyperbolic Plateaus of the Hénon Map

Rafael M. Frongillo*

January 24, 2010

Abstract

We describe an automated method for computing rigorous lower bounds for topological entropy which was originally introduced in [5]. We combine this method with the work of Arai in [1] to find rigorous lower bounds on topological entropy for 43 hyperbolic plateaus of the Hénon map. We also examine 15 area-preserving plateaus and compare our results with related work.

1 Introduction

Computers are proving increasingly useful in obtaining rigorous results in dynamics. Several computational methods have recently emerged to compute topological entropy bounds [3], [5], [8] and to prove hyperbolicity [1], [11]. In this paper we use the method of Day, Frongillo, and Treviño (DFT) [5] to compute lower bounds for topological entropy for the hyperbolic regions obtained by Arai in [1]. These structurally stable regions, called *hyperbolic plateaus*, have constant topological entropy, and thus we can bound the entropy on an entire region with a single lower bound computation.

Theorems 5.1 and 5.3 summarize our results. To our knowledge, all of these lower bounds are the largest known for their corresponding parameters. We selected the parameter regions so that the bounds obtained might give a global picture of the entropy of the Hénon map as a function of the parameters; see Figure 1 for such a picture.

This paper also demonstrates the effectiveness of the DFT approach, taking advantage of the fact that we are working in a familiar setting and can compare our results with what we expect. This is particularly the case for the area-preserving Hénon maps, which have been well-studied in the Physics community [10],[15],[6]. Recently, some precise rigorous results emerged as well [2]. We find that our rigorous lower bounds match or are very close to estimates given in previous work, and match the rigorous results exactly when applicable.

*University of California at Berkeley

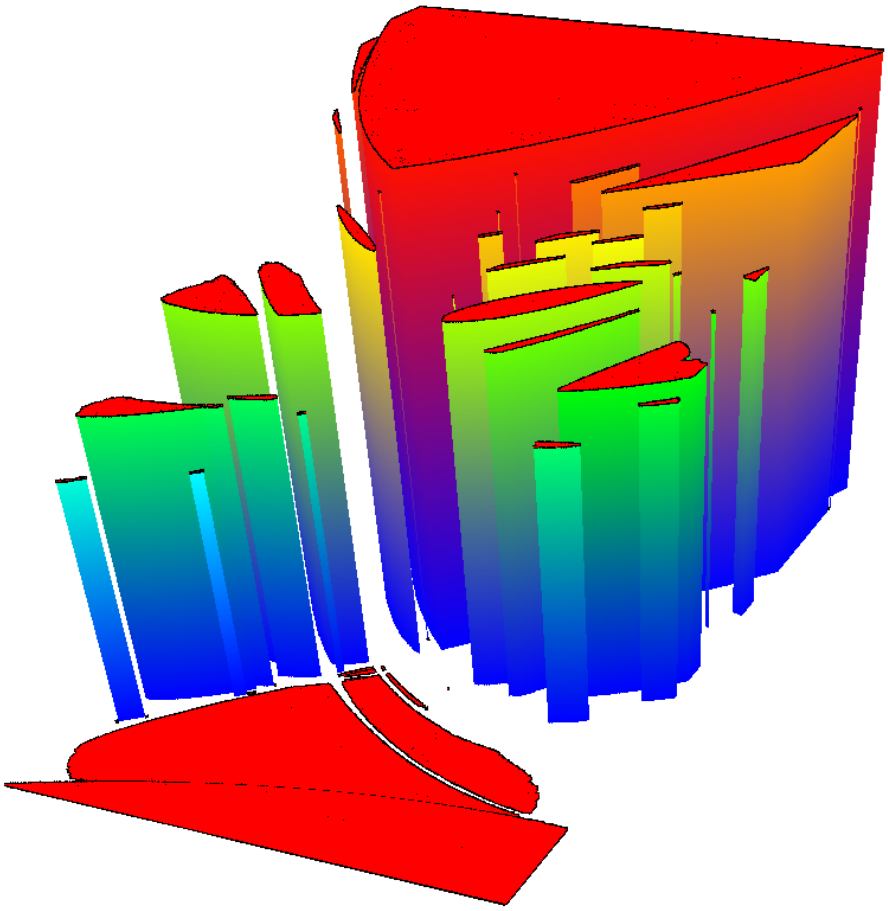

Figure 1: Rigorous lower bounds for topological entropy for the hyperbolic plateaus in Figure 4. The height of each plateau in the visualization is proportional to the entropy bound computed. See Theorem 5.1 or Figure 5 for the actual bounds.

2 Background

The DFT approach relies heavily on the Conley index, and we refer the reader to Section 2 of [5] for the relevant background. In Section 3 we will assume familiarity of basic symbolic dynamics; see e.g. [12]. The following briefly recalls definitions and basic theorems related to topological entropy and hyperbolicity.

2.1 Topological Entropy

We use topological entropy to measure the relative complexity of different dynamical systems. If the topological entropy of a dynamical system f, denoted $h(f)$, is positive, we say that f is *chaotic*.

Definition 2.1 (Topological entropy [12])**.** *Let $f : X \to X$ be a continuous map with respect to a metric d. We say that a set $W \subseteq X$ is (n, ε)-separated under f if for any distinct $x, y \in W$ we have $d\big(f^j(x),\ f^j(y)\big) > \varepsilon$ for some $0 \leq j < n$. The* topological entropy *of f is*

$$h(f) := \lim_{\varepsilon \to \infty} \limsup_{n \to \infty} \frac{log(s_f(n, \varepsilon))}{n}, \tag{1}$$

where $s_f(n, \varepsilon)$ denotes the maximum cardinality of an (n, ε)-separated set under f.

While topological entropy can be difficult to calculate in general, there is a simple formula for subshifts of finite type which is given in the following theorem. For a proof, see [12] or [14].

Theorem 2.2. *Let G be a directed graph with transition matrix A, and let (X_G, σ_G) be the corresponding subshift of finite type. Then the topological entropy of σ_G is $h(\sigma_G) = \log(sp(A))$, where $sp(A)$ denotes the spectral radius (maximum magnitude of an eigenvalue) of A.*

Theorem 2.3 ([14])**.** *Let f and g be continuous maps, and let ϕ be a semi-conjugacy from f to g. Then $h(f) \geq h(g)$.*

Note that if f and g are conjugate, Theorem 2.3 gives us $h(f) = h(g)$. In other words, topological entropy is invariant under conjugacy.

2.2 Hyperbolicity

To begin we define uniform hyperbolicity. Throughout the paper, we will refer to this property simply as hyperbolicity.

Definition 2.4 ([9])**.** *A map $f : X \to X$ is said to be (uniformly)* hyperbolic *if for every $x \in X$ the tangent space T_xX for f is a direct sum of stable and unstable subspaces. More precisely, we have $T_xX = E^s(x) \oplus E^u(x)$, where $E^s(x)$ and $E^u(x)$ satisfy the following inequalities for some $C > 0$ and $0 < \lambda < 1$, and for all $n \in \mathbb{N}$:*

1. *$\|Df^n(v)\| \leq C\lambda^n \|v\|$ for all $v \in E^s(x)$.*
2. *$\|Df^{-n}(v)\| \leq C\lambda^n \|v\|$ for all $v \in E^u(x)$.*

This structure can be thought of as a generalization of the structure of the Smale horseshoe, namely that there are invariant directions, and there is uniform contraction and expansion in the stable and unstable directions, respectively.

Some useful properties of hyperbolic systems are discussed below, but for more details see [14] and [9].

An important property of hyperbolic maps is that they are structurally stable [14], which implies that all maps in the same hyperbolic region are conjugate. Thus, by Theorem 2.3, the topological entropy is constant within such a region. For this reason, we will henceforth call these regions *hyperbolic plateaus*.

Hyperbolicity often makes it easier to identify interesting dynamics, but it is important to note that sometimes a system can be trivially hyperbolic. A helpful concept in this context is the *nonwandering set*.

Definition 2.5 ([14]). *The* nonwandering set *of a map f is the set of points x for which every neighborhood U of x has $f^n(U) \cap U \neq \emptyset$ for some $n \geq 1$.*

Automated methods for proving hyperbolicity have only been introduced recently, by Hruska [11] and Arai [1]. Arai uses a somewhat indirect technique to prove hyperbolicity which allows for more efficient computations than Hruska. Arai's technique, however, does not guarantee that the nonwandering set is not just a finite collection of periodic orbits, or even that it is nonempty. Specifically, Arai's technique does not give any information about the topological entropy of the regions in question, which is one motivation for computing entropy bounds for these regions.

3 Simplifying Subshifts

Given a subshift of finite type (X_G, σ_G) for a graph G, it is often of interest to know whether there is a graph H on fewer vertices such that (X_G, σ_G) and (X_H, σ_H) are conjugate. To this end, we recall the notion of strong shift equivalence.

Definition 3.1 (Strong shift equivalence). *Let A and B be matrices. An* elementary shift equivalence *between A and B is a pair (R, S) such that*

$$A = RS \text{ and } B = SR. \tag{2}$$

In this case, we write $(R, S) : A \to B$. If there is a sequence of such elementary shift equivalences $(R_i, S_i) : A_{i-1} \to A_i$, $1 \leq i \leq k$, we say that A_0 and A_k are strongly shift equivalent.

This notion is useful because of the following result due to R. F. Williams relating shift equivalence to symbolic dynamics.

Theorem 3.2 ([16]). *For directed graphs G and H, the corresponding subshifts (X_G, σ_G) and (X_H, σ_H) are conjugate if and only if the transition matrices of G and H are strongly shift equivalent.*

Theorem 3.2 allows us to prove that two subshifts are conjugate by a series of simple matrix computations. Finding matrices that give a strong shift equivalence, however, can be a very difficult problem. Two methods of finding

such equivalences are given in [12]: state splitting, where a single vertex is split into two, or state amalgamation, where two vertices are combined into one. In graph-theoretic terms, amalgamating two vertices is equivalent to contracting them, or contracting the edge between them. In general obtaining the smallest element of a strong shift equivalence class may involve both splittings and amalgamations. We instead focus on the simpler problem of obtaining H only by amalgamating vertices in G. This also has the advantage of producing a matrix that is more useful for our needs in this paper (see Section 4).

Let A be an $n \times n$ transition matrix with entries in $\{0, 1\}$. As we will show, the following two conditions, adapted from [12], allow us amalgamate vertices i and j.

$$\textbf{Forward Condition:} \quad A\vec{e}_i = A\vec{e}_j \text{ and } (\vec{e}_i^{\top} A) \cdot (\vec{e}_j^{\top} A) = 0 \tag{3}$$

$$\textbf{Backward Condition:} \quad \vec{e}_i^{\top} A = \vec{e}_j^{\top} A \text{ and } (A\vec{e}_i) \cdot (A\vec{e}_j) = 0 \tag{4}$$

Here $\vec{e}_i$ denotes the column vector with a 1 in position i and zeros elsewhere. From a graph-theoretic or dynamical systems point of view, the forward condition says that i and j have the same image but disjoint preimages, and the backward condition says they have the same preimage but disjoint images. See Figure 2 for an example.

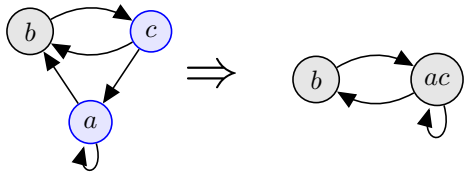

Figure 2: A forward amalgamation

Note that the backward condition for A is the same as the forward condition for $A^{\top}$. The following result allows us to reduce A to a smaller $n-1$ by $n-1$ matrix B if either of these conditions are satisfied for some pair of vertices. A somewhat different proof involving graph splittings is given in Chapter 2 of [12].

Theorem 3.3. *If i and j satisfy the forward condition (3) or backward condition (4) for a transition matrix A, then there is an elementary shift equivalence from A to the matrix obtained by amalgamating i and j.*

Proof. Let A be $n \times n$ and let

$$X = \left[\begin{array}{c|c} I_{j-1} & 0 \\ \hline \vec{0} & \vec{0} \\ \hline 0 & I_{n-j} \end{array}\right], \quad Y = \left[\begin{array}{c|c|c} I_{j-1} & \vec{e}_i & 0 \\ \hline 0 & \vec{0} & I_{n-j} \end{array}\right]. \tag{5}$$

Note that X and Y are $n \times n-1$ and $n-1 \times n$ matrices, respectively.

Assume the forward condition is satisfied for i and j in A. Then we obtain $B = YAX$ by amalgamating i and j. We will show that $(AX, Y) : A \to B$, or

in words, that AX and Y give an elementary shift equivalence from A to B. We have $(Y)(AX) = B$ immediately, so it remains to show $(AX)(Y) = A$. Note that

$$XY = \left[\begin{array}{c|c} I_{j-1} & 0 \\ \hline \vec{0} & \vec{0} \\ \hline 0 & I_{n-j} \end{array}\right] \left[\begin{array}{c|c|c} I_{j-1} & \vec{e}_i & 0 \\ \hline 0 & \vec{0} & I_{n-j} \end{array}\right] = \left[\begin{array}{c|c|c} I_{j-1} & \vec{e}_i & 0 \\ \hline \vec{0} & 0 & \vec{0} \\ \hline 0 & \vec{0} & I_{n-j} \end{array}\right], \quad (6)$$

and thus $AXY\vec{e}_k = A\vec{e}_k$ if $k \neq j$ and $AXY\vec{e}_j = A\vec{e}_i$. By the forward condition (3) we have $A\vec{e}_j = A\vec{e}_i$, so in fact $(AX)Y = A$.

Now assume instead that the backward condition is satisfied; we will show $(X^\top A, Y^\top) : A \to B$, where here $B = X^\top A Y^\top$. Again, $(X^\top A)(Y^\top) = B$ is trivial. By the remark above, i and j satisfy the forward condition for $A^\top$, and so by the above computation we have $A^\top XY = A^\top$. Thus $Y^\top(X^\top A) = (A^\top XY)^\top = (A^\top)^\top = A$. □

By applying Theorem 3.3 repeatedly, as long as there exist i, j satisfying either contraction condition, one can reduce A to a much smaller representative of its strong shift equivalence class; the resulting matrix B at the end of this process corresponds to a subshift (X_H, σ_H) which is therefore conjugate to (X_G, σ_G). Unfortunately it is shown in [7] that it is NP-hard (computationally intractable) to find an ordering of amalgamations which yields the smallest representative, but for small enough matrices a simple brute-force search is feasible.

4 Approach

Recall that our objective is to find good rigorous lower bounds on topological entropy for the Hénon maps, and also to demonstrate the effectiveness of the DFT method. Focusing on the hyperbolic parameters of the Hénon map allows us to accomplish both of these objectives simultaneously. Arai in [1] computed many hyperbolic plateaus for the Hénon map, and as discussed in Section 2, the topological entropy is constant on each plateau, so we get an entropy bound for a set of nonzero measure just by choosing a finite number of representatives. Moreover, the dynamics on the hyperbolic regions has been well-studied, especially in the area-preserving case, so we can evaluate our method by comparing our results to what we expect.

To obtain lower bounds on entropy, we compute a semi-conjugate symbolic dynamical system using the approach described in [5], which is ultimately based on the Conley index (again, we refer the reader to Section 2 of that paper for background). The technique consists of three main steps:

1. Discretize the phase space by overlaying a grid of boxes and compute a rigorous enclosure for the dynamics on these boxes.

2. Find a Conley index pair among the boxes and determine the Conley index for this pair using [13].

3. Compute a subshift from the index which is semi-conjugate to the original system.

This approach is very general, and in principle could be applied to systems of arbitrary dimension. A major benefit to using this method here, however, is that in our setting it is completely automated. As long as one knows roughly where in the phase space the invariant objects of interest are, one can simply plug in the parameters and compute. This complete automation allows us to compute entropy bounds for the Hénon map at many different parameter values without any extra manual effort. For this paper, a total of 58 parameter values were studied.

An advantage to studying hyperbolic parameters of Hénon when $|b| \leq 1$ is that the nonwandering set is disconnected. To see this, one can consider Plykin theory, as discussed in Chapter 7.9 of [14], from which we know that any connected trapping region (a region N with $f(N) \subset \text{int}(N)$) of the attractor has at least three holes. Considering a disc around such a hole, we see that since each hole must map strictly around another hole, an iterate of this disk must eventually expand, which contradicts the area-preserving or area-shrinking of the maps we are considering. Thus, all such trapping regions must be disconnected.

Since the nonwandering set is disconnected, we can bypass much of the complication in the second step of the DFT method, that of finding an index pair. This is because the invariant set will be naturally isolated; at a fine enough resolution, the collection of boxes that cover the invariant set will already be separated into disjoint regions.

We make two significant changes to the algorithms in [5]. The first is a method of scaling continuously between discretization resolutions. This approach stems from the observation that a $n \times n$ grid in the region $[1, 3] \times [1, 3]$ is functionally equivalent to a $2n \times 2n$ of region $[0, 4] \times [0, 4]$, provided that the nonwandering set lies completely within the first region. We will measure the resolution of a box covering $\mathcal{B}$ as the scaling factor between boxes in $\mathcal{B}$ and some fixed 'initial' box B_0 containing the nonwandering set. See Figure 3 for an illustration.

This continuous scaling allows us to get a better idea of how the entropy lower bound we compute varies with the resolution. By Theorem 9.6.1 of [14], there exists a finite Markov partition of the invariant set, and the fact that the nonwandering set is disconnected (see above) implies that in theory we can achieve this partition when our boxes are small enough. Thus we expect to obtain the true entropy value at a high enough resolution, and by seeing where the entropy levels off we can be confident, though not certian, that our lower bound is the actual value. This approach requires many more computations, but fortunately as stated above, the full automation of our approach allows us to do this with essentially no extra effort. For each of the 58 parameter values studied, we computed entropy bounds at between 64 and 72 different resolutions, yielding a total of over 3900 computations.

The second major addition to the algorithms is a final step where we simplify the subshift obtained from the DFT method through repeated applications of

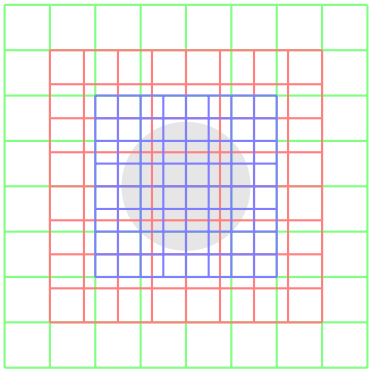

Figure 3: Three box coverings, with the grey circle representing the nonwandering set. Note that the blue could be obtained from subdividing the green, while the red is 'in-between' the other two. More precisely, if the outline of the blue grid is the initial box, the resolutions of the blue, red, and green grids are 4, 16/3, and 8 respectively.

Theorem 3.3, as described in Section 3. An important feature of the simplification is that the amalgamated subshift S' has a geometric interpretation just as the original subshift S did. Recall from [5] that for each symbol s_i we have a region N_i of the phase space, such that any trajectory $(\dots, s_{-2}, s_{-1}, s_0, s_1, s_2, \dots)$ in S corresponds to a trajectory in the original system through the regions $(\dots, N_{-2}, N_{-1}, N_0, N_1, N_2, \dots)$. In S', each symbol s'_i can be expressed as an amalgamation of symbols of S, and we take N'_i to be the union of the regions corresponding to these symbols. It is easy to see that the same trajectory property holds for S'. Thus we can vastly simplify our symbolic dynamical system while retaining a geometric interpretation of S'.

5 Results

5.1 Lower Bounds for Hyperbolic Plateaus of Hénon

We now apply the methods outlined in Section 4 to the real-valued Hénon map

$$f_{a,b}(x, y) = (a - x^2 + by, x)$$

for parameter values (a, b) such that $f_{a,b}$ is hyperbolic. Using the hyperbolic plateaus of Arai, we select representative parameter values to study for each plateau, as shown in Figure 4. The entropy bounds we compute constitute our main result, summarized in Theorem 5.1.

Theorem 5.1. *Let $F_i = \{f_{a,b} \mid (a, b) \in R_i\}$, where R_i is the ith plateau in Figure 4. Then for all i and all $f \in F_i$ we have $h(f) \geq h_i$, where the h_i are*

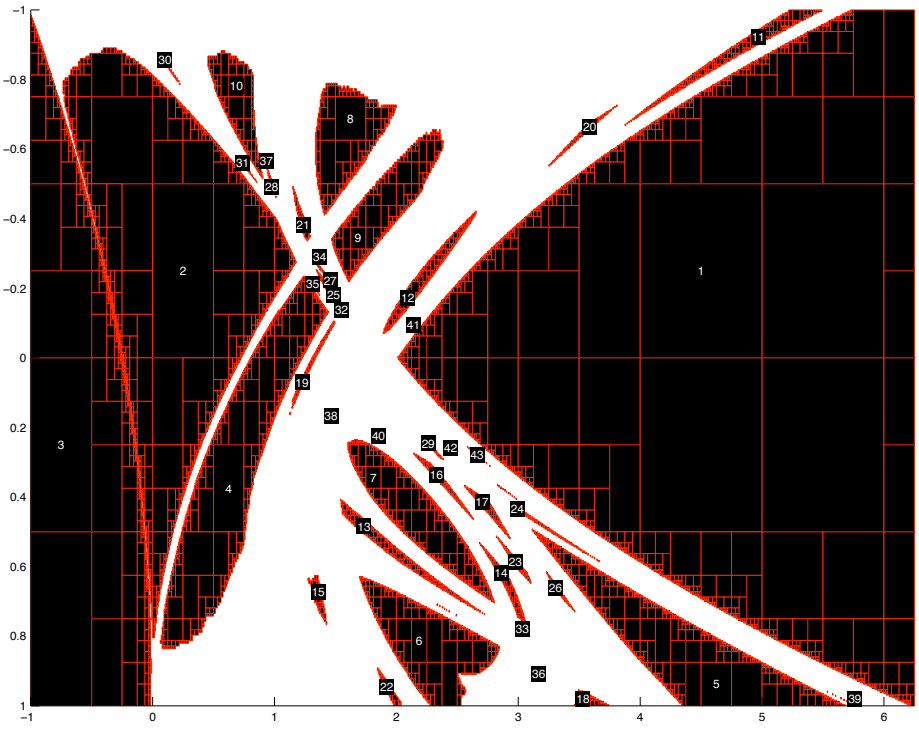

Figure 4: Hyperbolic plateaus for Hénon, as computed by Arai, with a on the horizontal axis and b on the vertical axis. The plateaus are labeled for reference, and each label is centered over the parameter values we use for its plateau.

defined below.

$$
\begin{array}{lllll}
h_1 = 0.6931 & h_5 = 0.6292 & h_6 = 0.4640 & h_7 = 0.5404 & h_8 = 0.5277 \\
h_9 = 0.5273 & h_{10} = 0.4334 & h_{11} = 0.6774 & h_{12} = 0.5967 & h_{13} = 0.5134 \\
h_{14} = 0.5550 & h_{15} = 0.4189 & h_{16} = 0.5723 & h_{17} = 0.5905 & h_{18} = 0.5193 \\
h_{20} = 0.6578 & h_{21} = 0.4296 & h_{22} = 0.4496 & h_{23} = 0.5809 & h_{24} = 0.6469 \\
h_{26} = 0.6076 & h_{28} = 0.4296 & h_{29} = 0.6088 & h_{30} = 0.3694 & h_{31} = 0.3504 \\
h_{33} = 0.5404 & h_{34} = 0.4035 & h_{36} = 0.4890 & h_{37} = 0.4296 & h_{39} = 0.6348 \\
h_{40} = 0.5546 & h_{41} = 0.6545 & h_{42} = 0.6289 & h_{43} = 0.6653 &
\end{array}
$$

Proof. For each R_i we selected $(a_i, b_i) \in R_i$ as a representative (these choices are shown in Figure 4). We then computed the map on boxes for f_{a_i,b_i} at different resolutions, and for each resolution we computed a rigorous lower bound for topological entropy using the DFT method; these bounds are summarized in Figure 6. Finally, by [1] we know each R_i is (uniformly) hyperbolic and so for each i we can apply the maximum lower bound achieved for (a_i, b_i) to all of R_i. □

Figure 1 and Figure 5 show an overview of our results. Note that the entropy

numbers shown are merely lower bounds, and not necessarily the true values. Since we are computing these bounds for hyperbolic parameter values, however, we know from Section 4 that if our entropy lower bound levels off as the grid resolution increases, we have strong evidence that we have obtained the correct value.

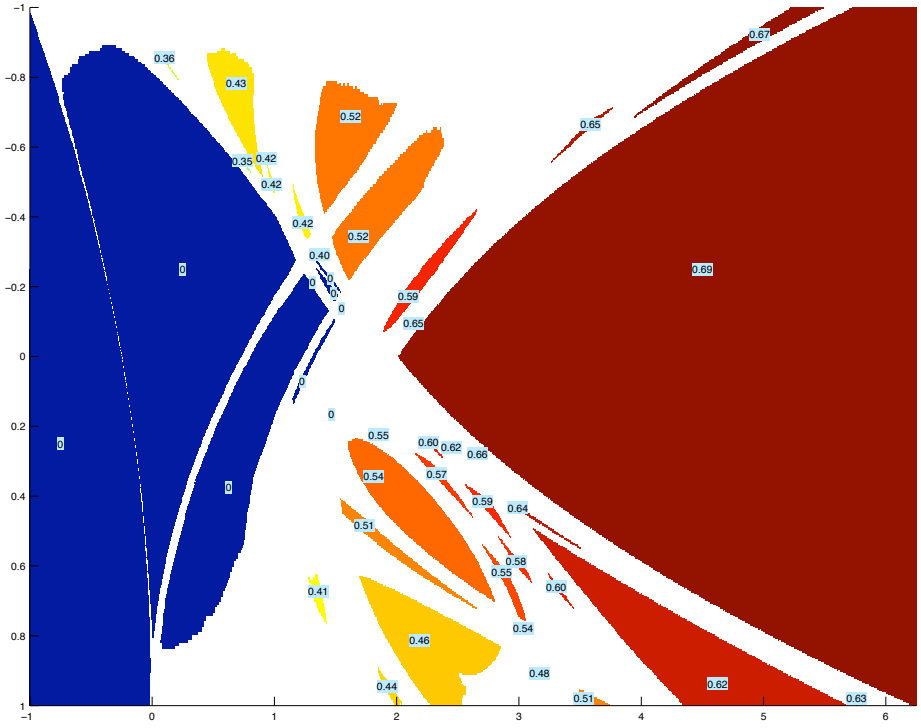

Figure 5: Rigorous lower bounds for topological entropy for the hyperbolic plateaus labeled 1 through 43 in Figure 4.

In Figure 6, we show plots of entropy bounds computed versus the resolution, for each of the 43 parameter values with a nonzero bound. Using the above heuristic, it seems that for most of the plateaus, the bounds we computed should be exact or very close. A few notable exceptions are plateaus 9, 10, 21, 28, 30, and 31, since the plots do not seem to have leveled off, and we would expect many of these bounds to improve with further computations. For plateaus 33, 34, 36, 37, and 39, it is unclear whether the plot has leveled off.

These plots also show some nice behavior of the DFT method. As we hoped, the entropy bound computed is roughly monotonic in the resolution, with few exceptions. While similar plots shown in [5] did not appear to be monotonic, it is likely that with a continuous resolution scaling like we use here, the bound would also increase roughly monotonically. This is beneficial behavior, as one would like the precision of the bound to increase with the precision of the box

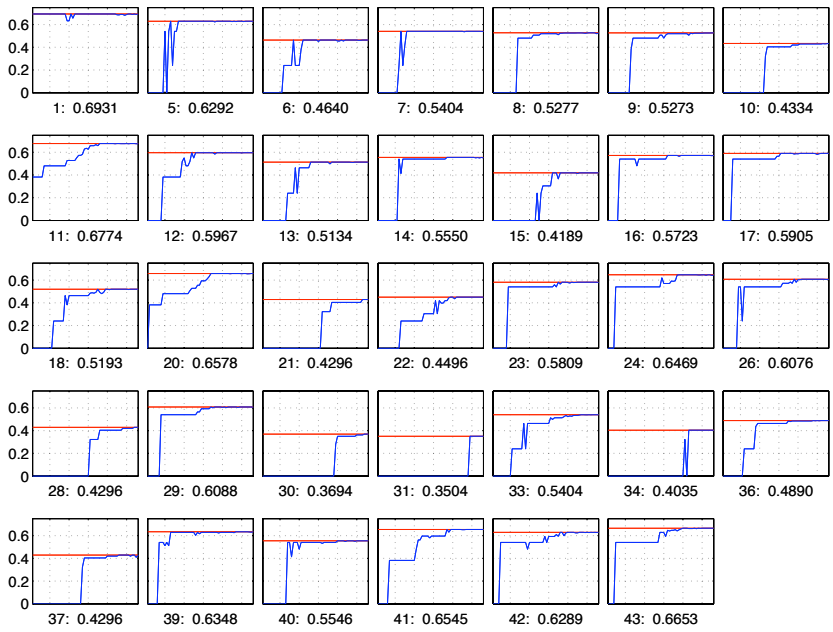

Figure 6: Each plot shows the entropy lower bound as a function of the resolution used. The red horizontal line in each represents the maximum lower bound computed, which is printed below the plot next to the plateau number. Plots are omitted for plateaus 2, 3, 4, 19, 25, 27, 32, 35, and 38, as the lower bounds computed for these plateaus were 0 for every resolution.

covering. Note however that typically the computation time grows with the resolution, so this increased precision is not without cost. Empirically, the running time seems to grow as d^r where d is the dimension of the invariant set, and r is the resolution.

While we have computed a large array of lower bounds, covering a vast portion of the parameter space of the Hénon map, a recent result of Arai gives a method of rigorously computing *exact* entropy values for (uniformly) hyperbolic Hénon [2]. In fact, in that work he computes values for plateaus numbered 5, 7, 11, and 12 in Figure 4, which match our lower bounds exactly. This new method is superior to that of DFT in the case we study here, and indeed it would be very interesting to use it to see which of our other bounds are tight, but as it relies heavily on hyperbolicity, it is not nearly as general. In particular, this new method could not be applied to the Hénon map for the classical parameter values, studied in [5], as the map is not uniformly hyperbolic for those parameters.

Assuming the lower bounds presented are at least close to the true values, Figure 5 suggests some sort of monotonicity of entropy as the parameters are varied. Specifically, it seems that entropy is roughly monotone along lines that

are perpendicular to the boundary of the maximal entropy plateau (plateau 1). One can also get an impression of the boundary of zero entropy for Hénon from these data.

5.2 Lower Bounds for the Area-Preserving Hénon Maps

When $b = -1$, the Hénon maps are area-preserving and orientation-preserving. This case has been well-studied, especially in the Physics literature. Starting in 1991, Davis, MacKay, and Sannami (DMS) [4] conjectured that Hénon was hyperbolic for three values of a (5.4, 5.59, 5.65) and conjectured symbolic dynamics for these three values as well. In 2002, de Carvalho and Hall in [6] replicated the results for $a = 5.4$ using a pruning approach. In 2004, Hagiwara and Shudo in [10] used a different pruning method to replicate all three of the values that DMS studied, and two more. They also give estimates of the topological entropy for $4 \leq a \leq 5.7$, which are displayed in Figure 8. Finally in 2007 some rigorous results appeared by Arai in [1], where he proved that there are 16 hyperbolic regions for $b = -1$, covering the parameters studied by DMS and the two others studied by Hagiwara and Shudo. Arai goes on in [2] to prove that the subshift conjectured by DMS for $a = 5.4$ is actually conjugate.

While our method cannot prove exact topological entropy values or conjugacies, we can attempt to verify that the entropy of the subshifts given in [4] are lower bounds, and perhaps show that the subshifts themselves are semi-conjugate. We focus first on the $a = 5.4$ case, where Davis, et al. conjectured that f_a is conjugate to the subshift corresponding to the following transition matrix T_{DMS}, which has topological entropy $h(T_{\text{DMS}}) = 0.6774$. Note that this is the same plateau as plateau 11 from the previous section.

$$T_{\text{DMS}} = \begin{array}{c} \\ N_1 \\ N_2 \\ N_3 \\ N_4 \\ N_5 \\ N_6 \\ N_7 \\ N_8 \end{array} \begin{array}{c} \begin{array}{cccccccc} N_1 & N_2 & N_3 & N_4 & N_5 & N_6 & N_7 & N_8 \end{array} \\ \left[\begin{array}{cccccccc} \mathbf{1} & \mathbf{1} & 0 & 0 & 0 & 0 & 0 & 0 \\ 0 & 0 & 0 & \mathbf{1} & \mathbf{1} & 0 & \mathbf{1} & 0 \\ 0 & 0 & 0 & \mathbf{1} & 0 & \mathbf{1} & 0 & \mathbf{1} \\ 0 & 0 & 0 & 0 & \mathbf{1} & 0 & 0 & 0 \\ \mathbf{1} & 0 & 0 & 0 & 0 & 0 & 0 & 0 \\ 0 & 0 & \mathbf{1} & \mathbf{1} & 0 & 0 & 0 & 0 \\ 0 & 0 & \mathbf{1} & 0 & 0 & \mathbf{1} & 0 & \mathbf{1} \\ 0 & 0 & 0 & \mathbf{1} & 0 & \mathbf{1} & 0 & \mathbf{1} \end{array}\right] \end{array} \tag{7}$$

Using our technique, we obtain a 42×42 symbol matrix T_{alg} which is semi-conjugate to $f_{5.4}$. The topological entropy of this matrix is the same value, $h(T_{\text{alg}}) = 0.6774$. The fact that $h(T_{\text{DMS}}) = h(T_{\text{alg}})$ suggests that the subshifts given by T_{DMS} and T_{alg} might be conjugate, and indeed we prove this in Theorem 5.2.

Theorem 5.2. *The subshift T_{DMS} in (7) is semi-conjugate to $f_{5.4}$, and moreover the symbols correspond to the regions labelled in Figure 7, which are the same regions conjectured by DMS.*

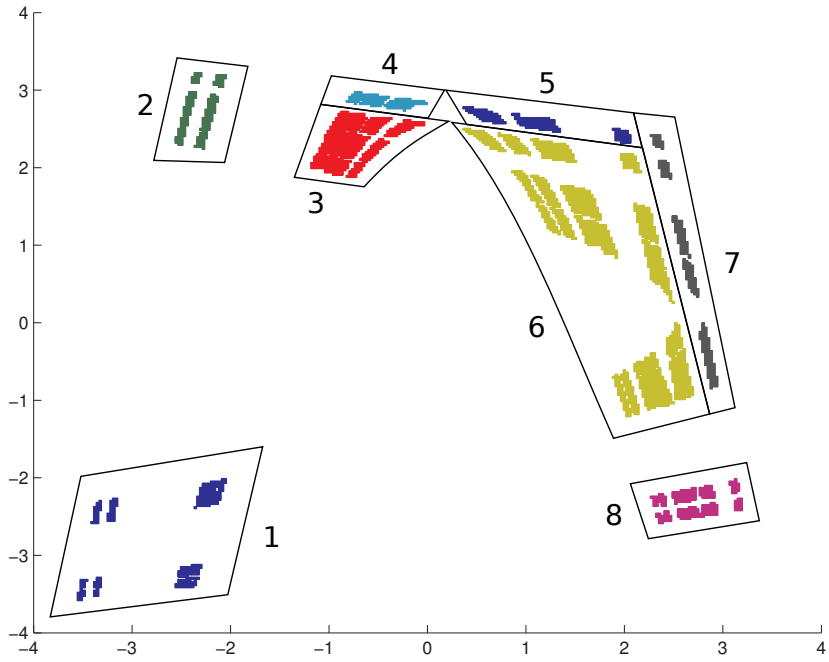

Figure 7: Index pair for $a = 5.4$ and $b = -1$, with regions colored to indicate the symbols for the smaller shift-equivalent symbol system.

Proof. By repeatedly applying Theorem 3.3 for the right choice of vertices, we obtain a strong shift equivalence between T_{DMS} and T_{alg}, which shows that the corresponding subshifts are indeed conjugate. Moreover, the contracted vertices can be chosen so that we obtain the same partition that was used by Davis, et al., which is shown in Figure 7, with the colored regions labeled so as to match the labels in (7) above. □

Our method also gives lower bounds which match the values conjectured by Davis, et al. for $a = 5.59$ and $a = 5.65$, as well as the value conjectured by Hagiwara and Shudo for $a = 4.58$. In addition to the these values, we also focus on 11 other values, which all together correspond to the first 15 area-preserving plateaus computed by Arai (the 16th is the maximal entropy plateau, which is plateau 1 in the previous section). Our results are summarized in the following theorem.

Theorem 5.3. *The following entropy bounds hold for the Hénon maps* $f_a =$

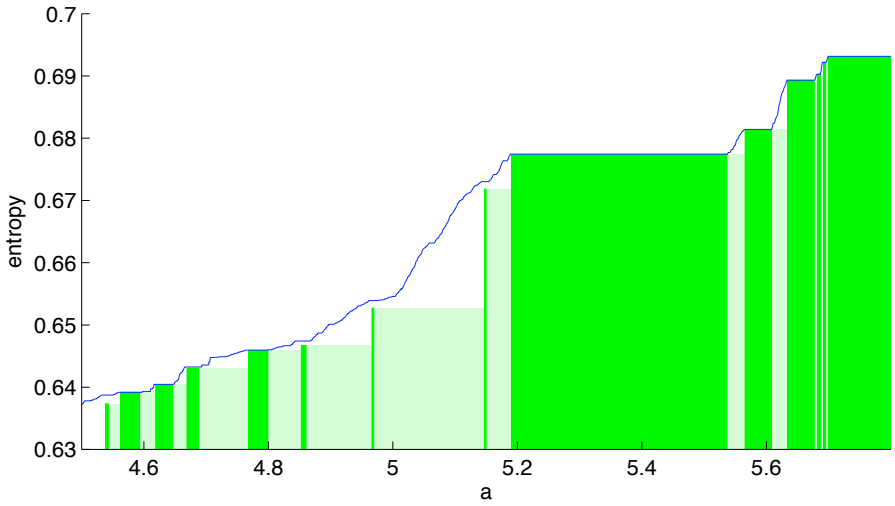

Figure 8: Topological entropy of the area-preserving Hénon maps, where $b = -1$. The estimates produced by Hagiwara and Shudo are in blue, and our rigorous lower bounds are in the darker green. The light green shows the lower bounds under the assumption of monotonicity.

$f_{a,-1}$. *Here we write* $h(f_{[a_0,a_1]}) \geq v$ *to mean* $\forall a \in [a_0, a_1], h(f_a) \geq v$.

1. $h\left(f_{[4.5383,\ 4.5386]}\right) \geq 0.6374$
2. $h\left(f_{[4.5388,\ 4.5430]}\right) \geq 0.6373$
3. $h\left(f_{[4.5624,\ 4.5931]}\right) \geq 0.6392$
4. $h\left(f_{[4.6189,\ 4.6458]}\right) \geq 0.6404$
5. $h\left(f_{[4.6694,\ 4.6881]}\right) \geq 0.6430$
6. $h\left(f_{[4.7682,\ 4.7993]}\right) \geq 0.6459$
7. $h\left(f_{[4.8530,\ 4.8604]}\right) \geq 0.6467$
8. $h\left(f_{[4.9666,\ 4.9692]}\right) \geq 0.6527$
9. $h\left(f_{[5.1470,\ 5.1497]}\right) \geq 0.6718$
10. $h\left(f_{[5.1904,\ 5.5366]}\right) \geq 0.6774$
11. $h\left(f_{[5.5659,\ 5.6078]}\right) \geq 0.6814$
12. $h\left(f_{[5.6343,\ 5.6769]}\right) \geq 0.6893$
13. $h\left(f_{[5.6821,\ 5.6858]}\right) \geq 0.6903$
14. $h\left(f_{[5.6859,\ 5.6860]}\right) \geq 0.6903$
15. $h\left(f_{[5.6917,\ 5.6952]}\right) \geq 0.6922$

Proof. Using the DFT method, we computed bounds for a single a value for each plateau; the representatives chosen were the following: 4.5385, 4.5409, 4.5800, 4.6323, 4.6788, 4.7838, 4.8600, 4.9679, 5.1483, 5.4000, 5.5900, 5.6500, 5.6839, 5.6859, 5.6934. Combining these bounds with the hyperbolic plateaus computed in [1], and using Theorem 2.3, we can extend the bounds to their corresponding plateau. □

Figure 8 shows a plot of the lower bounds from Theorem 5.3, shown against the estimates computed by Shudo and Hagiwara in [10]. The 4 cases discussed above correspond to plateaus 3, 10, 11, and 12. For these plateaus, our lower bounds match the estimates exactly, and our bounds for plateaus 4, 5, and 6 are very close. This is roughly what we expect given the plots shown in Figure 9. An

interesting trend we see in these data is that the algorithm performed better on the larger plateaus. This is perhaps because the stable and unstable manifolds seem to be more transverse the farther the parameters are from a bifurcation, thus making it easier to isolate the important regions of the phase space.

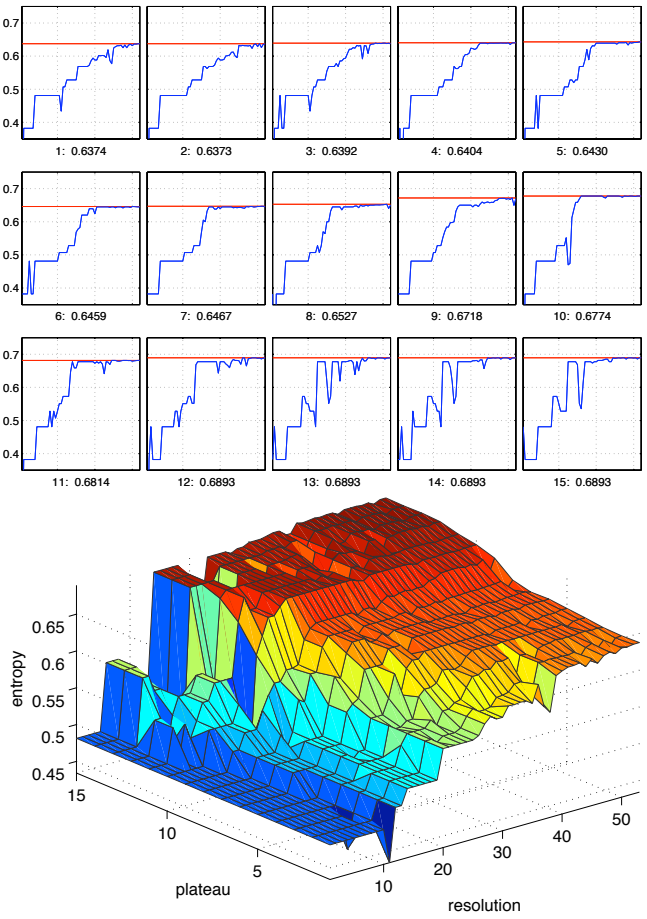

Figure 9: Entropy against resolution, as in Figure 6. The lower plot compares the 15 plots together to illustrate the monotonicity of the entropy we compute as we vary a, even at a fixed resolution.

6 Acknowledgements

The author would like to thank John Smillie for all of his guidance and advice, Zino Arai for sharing his useful data, Sarah Day and Rodrigo Treviño for their helpful comments, and Daniel Lepage for his help with the visualization in Figure 1.

References

[1] Zin Arai. On hyperbolic plateaus of the Hénon map. *Experiment. Math.*, 16(2):181–188, 2007.

[2] Zin Arai. On loops in the hyperbolic locus of the complex hénon map. Preprint, 2007.

[3] Wen-Chiao Cheng and Sheldon E. Newhouse. Pre-image entropy. *Ergodic Theory Dynam. Systems*, 25(4):1091–1113, 2005.

[4] M. J. Davis, R. S. MacKay, and A. Sannami. Markov shifts in the Hénon family. *Phys. D*, 52(2-3):171–178, 1991.

[5] Sarah Day, Rafael Frongillo, and Rodrigo Treviño. Algorithms for rigorous entropy bounds and symbolic dynamics. *SIAM Journal on Applied Dynamical Systems*, 7:1477–1506, 2008.

[6] André de Carvalho and Toby Hall. How to prune a horseshoe. *Nonlinearity*, 15(3):R19–R68, 2002.

[7] Rafael Frongillo. The hardness of state amalgamation in strong shift equivalence. Preprint, 2010.

[8] Zbigniew Galias. Interval methods for rigorous investigations of periodic orbits. *Internat. J. Bifur. Chaos Appl. Sci. Engrg.*, 11(9):2427–2450, 2001.

[9] John Guckenheimer and Philip Holmes. *Nonlinear oscillations, dynamical systems, and bifurcations of vector fields*, volume 42 of *Applied Mathematical Sciences*. Springer-Verlag, New York, 1990. Revised and corrected reprint of the 1983 original.

[10] Ryouichi Hagiwara and Akira Shudo. An algorithm to prune the area-preserving Hénon map. *J. Phys. A*, 37(44):10521–10543, 2004.

[11] Suzanne Lynch Hruska. A numerical method for constructing the hyperbolic structure of complex Hénon mappings. *Found. Comput. Math.*, 6(4):427–455, 2006.

[12] Douglas Lind and Brian Marcus. *An Introduction to Symbolic Dynamics and Coding*. Cambridge University Press, Cambridge, 1995.

[13] P. Pilarczyk. *Homology Computation-Software and Examples*. Jagiellonian University, 1998. (http://www.im.uj.edu.pl/∼pilarczy/homology.htm).

[14] Clark Robinson. *Dynamical systems*. Studies in Advanced Mathematics. CRC Press, Boca Raton, FL, 1995. Stability, symbolic dynamics, and chaos.

[15] D. Sterling, H. R. Dullin, and J. D. Meiss. Homoclinic bifurcations for the Hénon map. *Phys. D*, 134(2):153–184, 1999.

[16] R. F. Williams. Classification of subshifts of finite type. In *Recent advances in topological dynamics (Proc. Conf. Topological Dynamics, Yale Univ., New Haven, Conn., 1972; in honor of Gustav Arnold Hedlund)*, pages 281–285. Lecture Notes in Math., Vol. 318. Springer, Berlin, 1973.